Atomic-scale characterization of structural damage and recovery in Sn ion-implanted β-Ga_2O_3

Timothy Yoo[1], Xinyi Xia[2], Fan Ren[2], Alan Jacobs[3], Marko J. Tadjer[3], Stephen Pearton[1], and Honggyu Kim[1*]

[1] *Department of Materials Science and Engineering, University of Florida, Gainesville, FL 32611, USA*

[2] *Department of Chemical Engineering, University of Florida, Gainesville, FL 32611, USA*

[3] *U.S. Naval Research Laboratory, Washington DC 20375, USA*

[*] Electronic mail: honggyukim@ufl.edu

PLEASE CITE THIS ARTICLE AS DOI: 10.1063/5.0099915

Abstract

β-Ga_2O_3 is an emerging ultra-wide bandgap semiconductor, holding a tremendous potential for power-switching devices for next-generation high power electronics. The performance of such devices strongly relies on the precise control of electrical properties of β-Ga_2O_3, which can be achieved by implantation of dopant ions. However, a detailed understanding of the impact of ion implantation on the structure of β-Ga_2O_3 remains elusive. Here, using aberration-corrected scanning transmission electron microscopy, we investigate the nature of structural damage in ion-implanted β-Ga_2O_3 and its recovery upon heat treatment with the atomic-scale spatial resolution. We reveal that upon Sn ion implantation Ga_2O_3 films undergo a phase transformation from the monoclinic β-phase to the defective cubic spinel γ-phase which contains high-density antiphase boundaries. Using the planar defect models proposed for the γ-Al_2O_3, which has the same space group as β-Ga_2O_3, and atomic-resolution microscopy images, we identify that the observed antiphase boundaries are the {100}1/4<110> type in cubic structure. We show that post-implantation annealing at 1,100 °C under the N_2 atmosphere effectively recovers the β-phase; however, nano-sized voids retained within the β-phase structure and a γ-phase surface layer are identified as remanent damage. Our results offer an atomic-scale insight into the structural evolution of β-Ga_2O_3 under ion implantation and high-temperature annealing, which is key to the optimization of semiconductor processing conditions for relevant device design and the theoretical understanding of defect formation and phase stability.

Power electronics represents a technology that capitalizes on the use of power-switching devices for energy-efficient control of electric power. A key requirement of power-switching devices is high breakdown strength, which determines both the figure-of-merit and device performance limit.[1] As the breakdown voltage is scaled with the bandgap energy, semiconductors with a wide bandgap energy are needed to enable high voltage operation and reduce the power conversion loss for a given breakdown voltage.[2] The monoclinic, beta-phase (space group C2/m) Ga_2O_3 (β-Ga_2O_3) has therefore garnered tremendous interest as a promising contender for supporting next-generation power electronics due to its ultrawide bandgap of ~ 4.8 eV and theoretical breakdown electric field of ~ 8 MV cm^{-1}.[3–6] In addition, recent advances in bulk synthesis and thin-film technologies along with the availability of high-quality, cost-effective substrates have encouraged a surge in development of β-Ga_2O_3-based power devices for high-capacity power supplies, mass power transmission, and electric transportation.[7–11] These benefits have led to a demonstration of a range of β-Ga_2O_3-based power-switching devices, including Schottky diodes[12–14], metal-oxide-semiconductor field effect transistors (MOSFETs)[6,15–17], and metal-semiconductor field effect transistors (MESFETs)[18,19].

Critical to successful implementation of β-Ga_2O_3 in power-switching devices with the targeted performance is the precise control over its electrical properties via doping. Incorporation of dopant elements in β-Ga_2O_3 during film growth, often referred to as *in situ* doping[20], has been demonstrated using a variety of growth techniques such as Si, Ge, and Sn doping with molecular beam epitaxy (MBE)[21–23], Si and Sn doping with metal-organic vapor phase epitaxy (MOVPE)[24], and Sn doping with mist chemical vapor deposition (mist CVD), all of which result in n-type conductivity[25]. Delta doping of Si in β-Ga_2O_3, which leads to the formation of a two-dimensional electron gas, has been also attempted to fabricate MESFETs

with promising device performance.[18] Ion implantation is another powerful, well-established method to dope semiconductors with potential benefits, such as low temperature processing conditions and excellent doping profile and dosage control, which have been proven beneficial for fabricating power electronics based on Si and conventional wide bandgap semiconductors (GaN and SiC) over the last few decades.[26–28] Si ion implantation in β-Ga_2O_3 has been used to form low-resistance source/drain contacts.[29,30] In addition, deep acceptor levels can be created with Mg and N ion implantation in n-type β-Ga_2O_3 to define a high-resistance region for suppressing edge leakage current in vertical devices and achieving isolation of active device.[31–33] A major concern for the practicality of ion implantation is the structural damage induced by collisions between energetic dopant ions and host atoms as well as the effectiveness of post-implantation thermal annealing for damage recovery and dopant activation.[34] Prior work in Si and Sn ion implantation revealed that structural damage and remanent strain in β-Ga_2O_3 by x-ray diffraction (XRD) and transmission electron microscopy (TEM) that are not fully recovered with thermal annealing.[35] In addition, residual damage and the sign of stress in the irradiated layer depend on surface orientation of Si^+ implantation.[36] The accumulation of damage during ion irradiation also depends on the dose and ion flux density.[37–40] In the case of O_2 annealing, there was extensive redistribution of the Si, Ge, and Sn implanted ions across the entire dose range, while in sharp contrast, the use of N_2 annealing suppressed the dopant diffusion[41,42], which was ascribed to the influence of Ga vacancies[43]. Electron diffraction was used to show that Ge ion implantation induces a phase transformation of β-Ga_2O_3 to the κ-phase, a lesser-known subset of the ε-phase.[44,45] Early studies of radiation effects studies conducted on β polymorph show that amorphization does not occur at room temperature with low energy ions (*i.e.*, high percentage of displacement damage), even at high fluences.[39] Instead, the backscattered yield saturates at ~0.9,

due to the formation of point defects and defect clusters as well as the recombination of these defects, which lead to the saturation in observed damage.[39] The material is expected to become amorphous at low temperature due to accumulation of damage without dynamic annealing that occurs at room temperature, but this has not yet been demonstrated.

The current literature still lacks an atomic-scale investigation of the nature of implantation-induced structural damage and remanent defects after the thermal annealing process. This knowledge is vital to producing a fundamental understanding of the impact of structural defects on dopant diffusion/activation and achieving process optimization of ion implantation for desired electrical properties.

Here, we investigate the structural damage and recovery of Sn ion-implanted β-Ga_2O_3 films using aberration-corrected scanning transmission electron microscopy (STEM), which can resolve individual atomic columns with sub-Å spatial resolution. Using this atomic-resolution imaging technique, we find that the structural damage induced by Sn ion implantation is the γ-phase Ga_2O_3 (cubic, space group $Fd\bar{3}m$) featuring antiphase boundaries. High-temperature thermal annealing results in the recovery of the β-phase; however, remanent structural defects at different locations within the film are identified.

The 500 nm thick β-Ga_2O_3 epitaxial film was grown on an edge-defined, film-fed grown Fe-doped (010) β-Ga_2O_3 using ozone-assisted MBE, obtained from Novel Crystal Technology. In order to achieve a near-uniform Sn profile with the targeted concentration ~10^{19} cm^{-3}, the film was then implanted with Sn ions at 2x10^{13} cm^{-2}/60 keV + 3x10^{13} cm^{-2}/100keV + 4 x10^{13} cm^{-2}/200 keV. To minimize channeling of the implanted ions, implantation was performed 7 degrees off axis. The as-implanted film was then subject to a 60-second rapid thermal annealing at 1100 ˚C in N_2 ambient. Cross-sectional TEM specimens of as-grown, as-implanted, and post-

annealed samples were prepared for the $[001]_m$ projection of β-Ga_2O_3, where the subscript indicates the monoclinic structure, using an FEI Helios Nanolab 600 Dual Beam focused ion beam/scanning electron microscope (FIB/SEM). High-angle annular dark-field (HAADF) imaging in STEM was conducted on a Themis Z (Thermo Fisher Scientific) operated at 200 keV, equipped with a 5th order probe spherical aberration corrector. Energy dispersive x-ray spectroscopy (EDS) was performed using a Super-X detector system in a Themis Z. For HAADF-STEM imaging, an electron probe convergence semi-angle of 20 mrad and a HAADF detector range of 58 - 200 mrad were used. To minimize the image distortion arising from sample drift during imaging and enhance image contrast, HAADF-STEM images were obtained using the rigid registration method by which 20 fast-scan images were sequentially recorded, aligned using cross correlation, and averaged.

Figure 1(a) shows the representative HAADF-STEM image of an as-grown β-Ga_2O_3 film (unimplanted) imaged along the $[001]_m$ zone axis. As shown in the corresponding schematic in Fig. 1(b), this zone axis allows for imaging crystallographically inequivalent Ga_T and Ga_O positions, which have tetrahedral and octahedral coordination, respectively. Since the image intensity in HAADF-STEM images is sensitive to atomic number (Z), high-intensity region in Fig. 1(a) corresponds to the atomic columns consisting of the heavy constituent element (*i.e.*, Ga in β-Ga_2O_3), while the signal from oxygen atomic columns is barely detected.

Shown in Fig. 2(a) is the atomic-resolution HAADF-STEM image of a nominal β-Ga_2O_3 film after Sn ion implantation, *i.e.*, as-implanted Ga_2O_3, revealing unique atomic arrangements that are distinct from that of an unimplanted, as-grown β-Ga_2O_3. This implantation-induced damage region extends over ~ 120 nm from the film surface, which matches with the extent over which an appreciable number of Sn dopants (1 % of target concentration) are located in as-

implanted β-Ga_2O_3 (Fig. S1). Two distinct structural features are determined in this image. First, Figure 2(b) displays a hexagon-like feature, guided by the red hexagon, consisting of ten atomic columns with the high-intensity single atomic column in the center of each hexagon. This atomic arrangement corresponds to the γ-polymorph (cubic spinel) of Ga_2O_3 viewed along the $[110]_c$ projection, where the subscript refers to the cubic structure. The model structure used for constructing the γ-phase structure is based on magnetite, Fe_3O_4[46], containing cation vacancies, which adopts a defective spinel structure with the same space group ($Fd\bar{3}m$) as γ-Ga_2O_3, as suggested by Chang *et al* [47]. In this structure, the anion (oxygen) sublattice is fully occupied while the cation (Ga) sublattice contains vacancies that balance the [Ga]/[O] ratio to be 2/3 and lead to a small displacement of constituent atoms (thus termed "defective"). The structure of the γ-phase has not been extensively studied with regard to the bulk or film geometry as the β-phase is the most thermodynamically stable among reported polymorphs of Ga_2O_3; however, there have been reports on this cubic spinel structure in nanoparticles/nanocrystalline structures [48,49]. In addition, the presence of γ-phase inclusions was recently reported as a common structural defect in as-grown, doped β-Ga_2O_3 and alloyed β-$(Al_xGa_{1-x})_2O_3$ during film growth, especially at low temperature growth conditions.[47]

The second notable feature in as-implanted Ga_2O_3 is the defect phase, which is characterized by the diagonally streaking, high-intensity atomic columns and a succession of three atomic columns (triplets) in between those streaking atomic columns, marked by a red rectangle and a yellow arrow in Fig. 3(a), respectively. The atomic structure of this new defect phase does not match any projections from known polymorphs of Ga_2O_3, but rather resembles overlapped sheets of the γ-phase, that was previously observed in as-grown, doped β-Ga_2O_3.[47] Antiphase boundaries (APBs) were reported as a common planar defect in the defective spinel

structure (*e.g.*, γ-Al_2O_3 which has the same space group as γ-Ga_2O_3) that can produce lattice shifts.[50] The APBs for γ-Al_2O_3 that were experimentally determined using x-ray diffraction and conventional transmission electron microscopy analysis are characterized by the displacement vector 1/4<110>$_c$ in the $\{100\}_c$ planes of the cubic spinel structure.[50,51] Using this information, we constructed two model structures of the defect phase with the APBs of the type $(001)_c\ 1/4\,[10\bar{1}]_c$ [Figs. 3 (c,e)] and the type $(001)_c\ 1/4\,[\bar{1}0\bar{1}]_c$ [Figs. 3(d,f)], respectively. These types of APBs disrupt the coherence of the Ga sublattice while the oxygen sublattice remains unchanged.[50] We note that the high intensity atomic columns, as in the red box in Fig. 3(a), are due to Ga_O atoms stacked on top of each other from the overlapped sheets, as seen in Figs. 3(e,f), whereas the lower intensity triplets do not involve stacking by atoms from separate sheets. The model structures in Figs. 3(e,f) are in good agreement with the recorded HAADF-STEM images of an as-implanted Ga_2O_3 film, strongly suggesting that the structural origins for the dominant defect phase in as-implanted Ga_2O_3 are APBs.

Next, we examined the structural damage recovery of the implanted Ga_2O_3 film upon rapid thermal annealing. Figure 4(a) shows the low-magnification HAADF-STEM image of post-annealed Ga_2O_3. A large volume of damaged structure was recovered back to the β-phase. However, remanent structural defects persist. First, we observed low-intensity polygonal patches, marked by yellow arrows in Fig. 4(a), throughout the post-annealed film, mostly confined at 40-100 nm away from the surface. The high-magnification HAADF-STEM images in Fig. 4(b) revealed that the atomic structure within this low-intensity region mostly retains the β-phase structure. Thus, the relatively low intensities in the nominal Ga_T and Ga_O atomic columns in those polygonal regions arises from Ga vacancies, which is also supported by our EDS result (supplementary Fig. S2). While similar structural features have been reported in

prior literature as both vacancy clusters and voids[52–54], based on the size and low atomic density of polygonal patches observed in our work, we hereafter refer to those features as nano-sized voids. Furthermore, Sn dopants were identified in the vicinity of these nano-sized voids. Since the Sn dopants have a higher Z than the host (Ga), the Sn-containing Ga atomic columns show higher intensities in HAADF-STEM images. Figures 4(c, d) show a high-magnification HAADF-STEM image near a nano-sized void and a corresponding atomic-column intensity map. Using the statistical criterion used in previous studies[55,56], atomic columns having distinctly higher intensities than those of neighboring atomic columns are marked by white arrows. Given that these atomic columns are atomically isolated, it is highly likely that high image intensities arise from heavy Sn dopants rather than a gradual change in number of Ga atoms across the interface between nano-sized voids and β-Ga_2O_3. As shown in Figs. 4(c,d), Sn dopants, indicated by white arrows, are predominantly located at the octahedral coordinated Ga atomic columns (Ga_O), which is consistent with previous theoretical prediction[57,58] and experimental results[47,59].

Another major feature in post-annealed Ga_2O_3 is the incomplete recovery of the β-phase near the surface of the Ga_2O_3 film. Figure 4(e) shows the combination of the pure γ-phase structure and the defect phase similar to the as-implanted Ga_2O_3, shown in Figs. 2 and 3. This remanent γ-phase extends about 5-10 nm from the film surface, which is consistent with the thickness of the remaining defect layer observed in post-annealed Ge, Sn, and Si implanted β-Ga_2O_3 films [35,41], although these early studies did not identify the nature of this surface layer. Note that, in prior studies, the formation of the γ-phase has been observed at the surface of the β-Ga_2O_3 during film growth [47,60]. Moreover, as mentioned earlier, the γ-phase has been identified in nanostructures[48,49], where the surface-to-volume ratio is high. These experimental results

along with our observation of the γ-phase on the surface suggest that the surface energy plays an important role in the stability of the γ-phase over the β-phase. Current theoretical studies on the surface energies of Ga_2O_3 polymorphs are limited to the β-phase[61,62], thus it would be interesting to computationally investigate the landscape of surface energies of different polymorphs of Ga_2O_3 with respect to crystallographic planes and annealing conditions.

It is worth noting that HAADF-STEM imaging is less sensitive to light elements than relatively heavy elements (*e.g.*, oxygen in Ga_2O_3). However, given the extent (4 – 20 nm) and atomic structure of the detected nano-sized voids observed in Fig. 4(a), it is believed that this region may contain oxygen vacancies as well to maintain reasonable stoichiometry with local charge neutrality. Clustering of cation and anion vacancies was previously reported for implanted and annealed wide bandgap semiconductors, such as GaN.[63] These nano-sized voids are typically formed when vacancies are mobile and there are no sinks such as dislocations and free surface. Based on our result showing that no clusters were observed near the top 40 nm of the thin film, we speculate that the vacancies present in the γ-phase (as-implanted structure) are annealed to the surface but those present at deeper region within the film agglomerate into a stable nano-sized void. Further systematic computational investigations are needed to produce an improved understanding of the mechanisms of vacancy clustering (and Sn ion segregation near nano-sized voids) and its impact on the electronic properties of β-Ga_2O_3. Additionally, another imaging technique available in STEM, namely annular bright-field (ABF) imaging, which has been used to detect light elements (*i.e.*, oxygen) in β-Ga_2O_3[64], may prove useful in future studies for locating regions of dopant segregation. As demonstrated in Fig. S3, ABF-STEM imaging is sensitive to relatively light concentrations of dopants, especially heavy dopants like Sn in β-Ga_2O_3. Quantitative analysis of both ABF and HAADF images in

combination with image simulation is needed to further elucidate the evolution of point defects in Ga_2O_3 after implantation and post thermal annealing.

To summarize, we have performed HAADF imaging in an aberration-corrected STEM to investigate the impact of high-energy ion implantation and rapid thermal annealing on the structure of β-Ga_2O_3. We identified that Sn ion implantation induces the phase transformation from the β-phase to the γ-phase with high density of the defect phase. This result is in stark contrast to the reported phase transformation of Ge-implanted β-Ga_2O_3, where the β-phase is transformed into the κ-phase.[45] The origin of the defect phase in the γ-phase was determined to be APBs on $\{100\}_c$ planes with the lattice displacement of ¼$\langle 110\rangle_c$. High-temperature rapid thermal annealing was proven effective to recover the β-phase from the defective γ-phase; however, nano-sized voids embedded in β-Ga_2O_3 and the γ-phase on the film surface were identified as remanent structural defects. These are likely the structural origins for incomplete recovery of the lattice parameters and increased XRD rocking curve full width at half maximum that are observed in Sn ion implanted β-Ga_2O_3 after annealing.[35] The atomic-scale insights into the structure/defect evolution presented in this work provide invaluable constraints for future theoretical studies on the formation and diffusion of point defects (vacancies and dopants) and the phase stability of competing polymorphs (β- and γ-phases). In addition, our results emphasize the need to optimize the conditions for implantation and annealing. In particular, approaches to avoid the formation of the surface γ-phase are urgently needed as the properties of this region, which interfaces source/drain contacts, diode junctions, and channels, have profound influence on the performance of power-switching devices.

Supplementary Material

See supplementary material (link added by the publisher) for the secondary ion mass spectroscopy (SIMS) of the Sn profile, the EDS line profile across the nano-sized void, and ABF-STEM results.

Acknowledgements

This work was funded by the Defense Threat Reduction Agency (DTRA) as part of the Interaction of Ionizing Radiation with Matter University Research Alliance (IIRM-URA) under contract number HDTRA1-20-2-0002. The work at UF was also supported by the NSF DMR 1856662 (James Edgar). The part of the microscopy work was supported by the Research Opportunity Seed Fund (ROSF) from the University of Florida. Research at NRL was supported by the Office of Naval Research (ONR).

No conflicts of interest

The authors have no conflicts to disclose.

Figure Captions

Figure 1: (a) HAADF-STEM image of a β-Ga_2O_3 film imaged along $[001]_m$, where the subscript indicates the monoclinic structure. (b) Schematic of β-Ga_2O_3 corresponding to the region in (a), marked by the yellow dotted box. Ga_T and Ga_O have tetrahedral and octahedral coordination, respectively.

Figure 2: (a) HAADF-STEM image of a nominal Ga_2O_3 film implanted with Sn ions. (b) Schematic (top) and high-magnification HAADF-STEM image (bottom) of the γ-Ga_2O_3 structure projected along $[110]_c$, where the subscript indicates the cubic structure. Locations of the pure γ-Ga_2O_3 are indicated by yellow arrows in (a).

Figure 3: (a, b) High-magnification HAADF-STEM images of a nominal Ga_2O_3 film implanted with Sn ions. (c, d) Projected unit cells of a cubic spinel structure along $[110]_c$ that represent the lattice shifts, $1/4\,[10\bar{1}]_c$ and $1/4\,[\bar{1}0\bar{1}]_c$, respectively. (e, f) Projected model structures along $[110]_c$ constructed based on the lattice shifts in (c, d), which match the recorded HAADF-STEM images in (a, b).

Figure 4: (a) Low-magnification HAADF-STEM image of post-annealed Ga_2O_3 showing low-intensity polygonal patches, marked by the yellow arrows. (b) High-magnification HAADF-STEM image of one of polygonal patch demonstrating that the polygonal patch retains the β-phase with low intensities in the nominal Ga_T and Ga_O atomic columns, indicative of Ga vacancies. (c) High-magnification HAADF-STEM and (d) corresponding atomic column intensity map revealing Sn dopants, located in the nominal Ga_O sites, in the vicinity of the nano-sized void, which is evidenced

by higher intensities than their neighboring Ga atomic columns (see white arrows). (e) HAADF-STEM image of the remanent γ-phase near the surface of the film after rapid thermal annealing.

Reference

[1] K. Shenai, IEEE Transactions on Electron Devices **65**, 4216 (2018).
[2] B.J. Baliga, Journal of Applied Physics **53**, 1759 (1982).
[3] T. Onuma, S. Saito, K. Sasaki, T. Masui, T. Yamaguchi, T. Honda, and M. Higashiwaki, Jpn. J. Appl. Phys. **54**, 112601 (2015).
[4] M. Higashiwaki and G.H. Jessen, Appl. Phys. Lett. **112**, 060401 (2018).
[5] S.J. Pearton, J. Yang, P.H. Cary, F. Ren, J. Kim, M.J. Tadjer, and M.A. Mastro, Applied Physics Reviews **5**, 011301 (2018).
[6] S. Sharma, K. Zeng, S. Saha, and U. Singisetti, IEEE Electron Device Letters **41**, 836 (2020).
[7] G. Wagner, M. Baldini, D. Gogova, M. Schmidbauer, R. Schewski, M. Albrecht, Z. Galazka, D. Klimm, and R. Fornari, Physica Status Solidi (a) **211**, 27 (2014).
[8] Z. Galazka, R. Uecker, D. Klimm, K. Irmscher, M. Naumann, M. Pietsch, A. Kwasniewski, R. Bertram, S. Ganschow, and M. Bickermann, ECS J. Solid State Sci. Technol. **6**, Q3007 (2016).
[9] S.J. Pearton, F. Ren, M. Tadjer, and J. Kim, Journal of Applied Physics **124**, 220901 (2018).
[10] M. Higashiwaki, Physica Status Solidi (RRL) – Rapid Research Letters **15**, 2100357 (2021).
[11] A.J. Green, J. Speck, G. Xing, P. Moens, F. Allerstam, K. Gumaelius, T. Neyer, A. Arias-Purdue, V. Mehrotra, A. Kuramata, K. Sasaki, S. Watanabe, K. Koshi, J. Blevins, O. Bierwagen, S. Krishnamoorthy, K. Leedy, A.R. Arehart, A.T. Neal, S. Mou, S.A. Ringel, A. Kumar, A. Sharma, K. Ghosh, U. Singisetti, W. Li, K. Chabak, K. Liddy, A. Islam, S. Rajan, S. Graham, S. Choi, Z. Cheng, and M. Higashiwaki, APL Materials **10**, 029201 (2022).
[12] W. Li, Z. Hu, K. Nomoto, Z. Zhang, J.-Y. Hsu, Q.T. Thieu, K. Sasaki, A. Kuramata, D. Jena, and H.G. Xing, Appl. Phys. Lett. **113**, 202101 (2018).
[13] J. Yang, F. Ren, M. Tadjer, S.J. Pearton, and A. Kuramata, ECS J. Solid State Sci. Technol. **7**, Q92 (2018).
[14] K. Konishi, K. Goto, H. Murakami, Y. Kumagai, A. Kuramata, S. Yamakoshi, and M. Higashiwaki, Appl. Phys. Lett. **110**, 103506 (2017).
[15] K. Zeng, A. Vaidya, and U. Singisetti, Appl. Phys. Express **12**, 081003 (2019).
[16] K. Zeng, A. Vaidya, and U. Singisetti, IEEE Electron Device Letters **39**, 1385 (2018).
[17] A.J. Green, K.D. Chabak, M. Baldini, N. Moser, R. Gilbert, R.C. Fitch, G. Wagner, Z. Galazka, J. Mccandless, A. Crespo, K. Leedy, and G.H. Jessen, IEEE Electron Device Letters **38**, 790 (2017).
[18] Z. Xia, C. Joishi, S. Krishnamoorthy, S. Bajaj, Y. Zhang, M. Brenner, S. Lodha, and S. Rajan, IEEE Electron Device Letters **39**, 568 (2018).
[19] Z. Xia, H. Xue, C. Joishi, J. Mcglone, N.K. Kalarickal, S.H. Sohel, M. Brenner, A. Arehart, S. Ringel, S. Lodha, W. Lu, and S. Rajan, IEEE Electron Device Letters **40**, 1052 (2019).
[20] Z. Feng, A.F.M.A.U. Bhuiyan, N.K. Kalarickal, S. Rajan, and H. Zhao, Appl. Phys. Lett. **117**, 222106 (2020).
[21] A. Mauze, Y. Zhang, T. Itoh, E. Ahmadi, and J.S. Speck, Appl. Phys. Lett. **117**, 222102 (2020).
[22] N.K. Kalarickal, Z. Xia, J. McGlone, S. Krishnamoorthy, W. Moore, M. Brenner, A.R. Arehart, S.A. Ringel, and S. Rajan, Appl. Phys. Lett. **115**, 152106 (2019).
[23] E. Ahmadi, O.S. Koksaldi, S.W. Kaun, Y. Oshima, D.B. Short, U.K. Mishra, and J.S. Speck, Appl. Phys. Express **10**, 041102 (2017).
[24] M. Baldini, M. Albrecht, A. Fiedler, K. Irmscher, R. Schewski, and G. Wagner, ECS J. Solid State Sci. Technol. **6**, Q3040 (2017).
[25] S. Lee, K. Kaneko, and S. Fujita, Jpn. J. Appl. Phys. **55**, 1202B8 (2016).

[26] J.C. Zolper, Journal of Crystal Growth **178**, 157 (1997).
[27] J.S. Williams, Materials Science and Engineering: A **253**, 8 (1998).
[28] S.O. Kucheyev, J.S. Williams, and S.J. Pearton, Materials Science and Engineering: R: Reports **33**, 51 (2001).
[29] M.H. Wong, Y. Nakata, A. Kuramata, S. Yamakoshi, and M. Higashiwaki, Appl. Phys. Express **10**, 041101 (2017).
[30] K. Sasaki, M. Higashiwaki, A. Kuramata, T. Masui, and S. Yamakoshi, Appl. Phys. Express **6**, 086502 (2013).
[31] M.H. Wong, H. Murakami, Y. Kumagai, and M. Higashiwaki, IEEE Electron Device Letters **41**, 296 (2020).
[32] M.H. Wong, C.-H. Lin, A. Kuramata, S. Yamakoshi, H. Murakami, Y. Kumagai, and M. Higashiwaki, Appl. Phys. Lett. **113**, 102103 (2018).
[33] K. Tetzner, A. Thies, E. Bahat Treidel, F. Brunner, G. Wagner, and J. Würfl, Appl. Phys. Lett. **113**, 172104 (2018).
[34] A. Nikolskaya, E. Okulich, D. Korolev, A. Stepanov, D. Nikolichev, A. Mikhaylov, D. Tetelbaum, A. Almaev, C.A. Bolzan, A. Buaczik, R. Giulian, P.L. Grande, A. Kumar, M. Kumar, and D. Gogova, Journal of Vacuum Science & Technology A **39**, 030802 (2021).
[35] M.J. Tadjer, C. Fares, N.A. Mahadik, J.A. Freitas, D. Smith, R. Sharma, M.E. Law, F. Ren, S.J. Pearton, and A. Kuramata, ECS J. Solid State Sci. Technol. **8**, Q3133 (2019).
[36] V. Trushin, A. Nikolskaya, D. Korolev, A. Mikhaylov, A. Belov, E. Pitirimova, D. Pavlov, and D. Tetelbaum, Materials Letters **319**, 132248 (2022).
[37] A. Azarov, C. Bazioti, V. Venkatachalapathy, P. Vajeeston, E. Monakhov, and A. Kuznetsov, Phys. Rev. Lett. **128**, 015704 (2022).
[38] A. Azarov, V. Venkatachalapathy, E.V. Monakhov, and A.Yu. Kuznetsov, Appl. Phys. Lett. **118**, 232101 (2021).
[39] E. Wendler, E. Treiber, J. Baldauf, S. Wolf, and C. Ronning, Nuclear Instruments and Methods in Physics Research Section B: Beam Interactions with Materials and Atoms **379**, 85 (2016).
[40] S.B. Kjeldby, A. Azarov, P.D. Nguyen, V. Venkatachalapathy, R. Mikšová, A. Macková, A. Kuznetsov, Ø. Prytz, and L. Vines, Journal of Applied Physics **131**, 125701 (2022).
[41] R. Sharma, M.E. Law, M. Xian, M. Tadjer, E.A. Anber, D. Foley, A.C. Lang, J.L. Hart, J. Nathaniel, M.L. Taheri, F. Ren, S.J. Pearton, and A. Kuramata, Journal of Vacuum Science & Technology B **37**, 051204 (2019).
[42] R. Sharma, M.E. Law, C. Fares, M. Tadjer, F. Ren, A. Kuramata, and S.J. Pearton, AIP Advances **9**, 085111 (2019).
[43] Y.K. Frodason, P. Krzyzaniak, L. Vines, J. Varley, C. Van de Walle, and K.M. Johansen, Bulletin of the American Physical Society (2022).
[44] I. Cora, F. Mezzadri, F. Boschi, M. Bosi, M. Čaplovičová, G. Calestani, I. Dódony, B. Pécz, and R. Fornari, CrystEngComm **19**, 1509 (2017).
[45] E.A. Anber, D. Foley, A.C. Lang, J. Nathaniel, J.L. Hart, M.J. Tadjer, K.D. Hobart, S. Pearton, and M.L. Taheri, Appl. Phys. Lett. **117**, 152101 (2020).
[46] H.St.C. O'Neill and W.A. Dollase, Phys Chem Minerals **20**, 541 (1994).
[47] C.S. Chang, N. Tanen, V. Protasenko, T.J. Asel, S. Mou, H.G. Xing, D. Jena, and D.A. Muller, APL Materials **9**, 051119 (2021).
[48] Helen.Y. Playford, A.C. Hannon, M.G. Tucker, D.M. Dawson, S.E. Ashbrook, R.J. Kastiban, J. Sloan, and R.I. Walton, J. Phys. Chem. C **118**, 16188 (2014).

[49] O. Nikulina, D. Yatsenko, O. Bulavchenko, G. Zenkovets, and S. Tsybulya, Zeitschrift Für Kristallographie - Crystalline Materials **231**, 261 (2016).
[50] M. Rudolph, M. Motylenko, and D. Rafaja, IUCrJ **6**, 116 (2019).
[51] A. Dauger and D. Fargeot, Radiation Effects (2006).
[52] A. Meldrum, S. Honda, C.W. White, R.A. Zuhr, and L.A. Boatner, J. Mater. Res. **16**, 2670 (2001).
[53] J.M. Polfus, O.M. Løvvik, R. Bredesen, and T. Peters, Acta Materialia **195**, 708 (2020).
[54] C. Bazioti, V.S. Olsen, A.Y. Kuznetsov, L. Vines, and Ø. Prytz, Phys. Chem. Chem. Phys. **22**, 3779 (2020).
[55] H. Kim, J.Y. Zhang, S. Raghavan, and S. Stemmer, Phys. Rev. X **6**, 041063 (2016).
[56] J. Hwang, J.Y. Zhang, A.J. D'Alfonso, L.J. Allen, and S. Stemmer, Phys. Rev. Lett. **111**, 266101 (2013).
[57] J.B. Varley, J.R. Weber, A. Janotti, and C.G. Van de Walle, Appl. Phys. Lett. **97**, 142106 (2010).
[58] S. Lany, APL Materials **6**, 046103 (2018).
[59] S.C. Siah, R.E. Brandt, K. Lim, L.T. Schelhas, R. Jaramillo, M.D. Heinemann, D. Chua, J. Wright, J.D. Perkins, C.U. Segre, R.G. Gordon, M.F. Toney, and T. Buonassisi, Appl. Phys. Lett. **107**, 252103 (2015).
[60] H.M. Jeon, K.D. Leedy, D.C. Look, C.S. Chang, D.A. Muller, S.C. Badescu, V. Vasilyev, J.L. Brown, A.J. Green, and K.D. Chabak, APL Materials **9**, 101105 (2021).
[61] J. Lee, S. Ganguli, A.K. Roy, and S.C. Badescu, J. Chem. Phys. **150**, 174706 (2019).
[62] S. Mu, M. Wang, H. Peelaers, and C.G. Van de Walle, APL Materials **8**, 091105 (2020).
[63] M. Maekawa, A. Miyashita, S. Sakai, and A. Kawasuso, Phys. Rev. B **102**, 054427 (2020).
[64] H.-C. Huang, M. Kim, X. Zhan, K. Chabak, J.D. Kim, A. Kvit, D. Liu, Z. Ma, J.-M. Zuo, and X. Li, ACS Nano **13**, 8784 (2019).

AIP Publishing

Applied Physics Letters ACCEPTED MANUSCRIPT

This is the author's peer reviewed, accepted manuscript. However, the online version of record will be different from this version once it has been copyedited and typeset.

PLEASE CITE THIS ARTICLE AS DOI: 10.1063/5.0099915

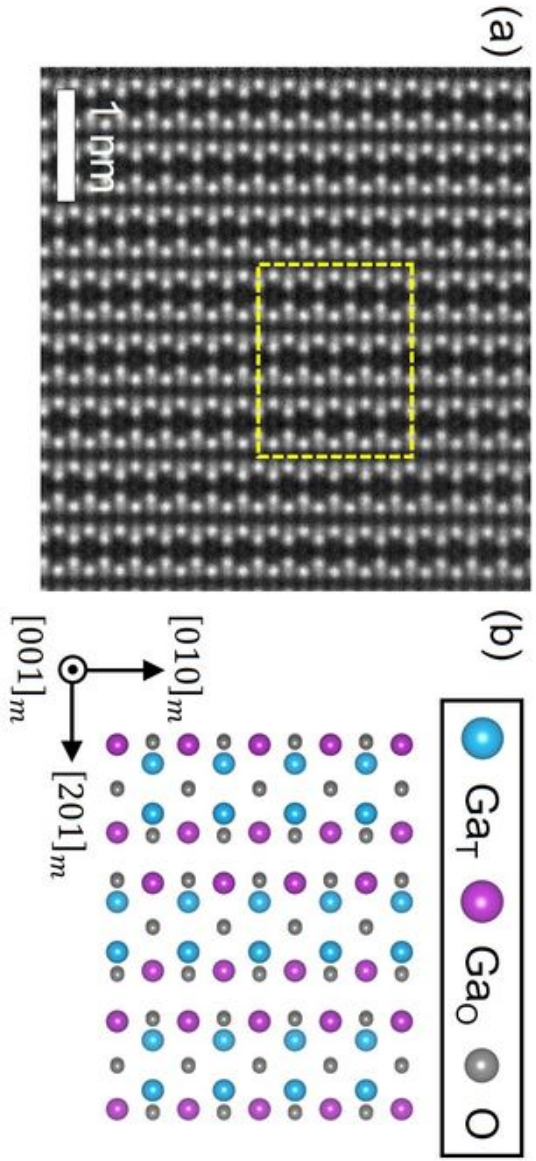

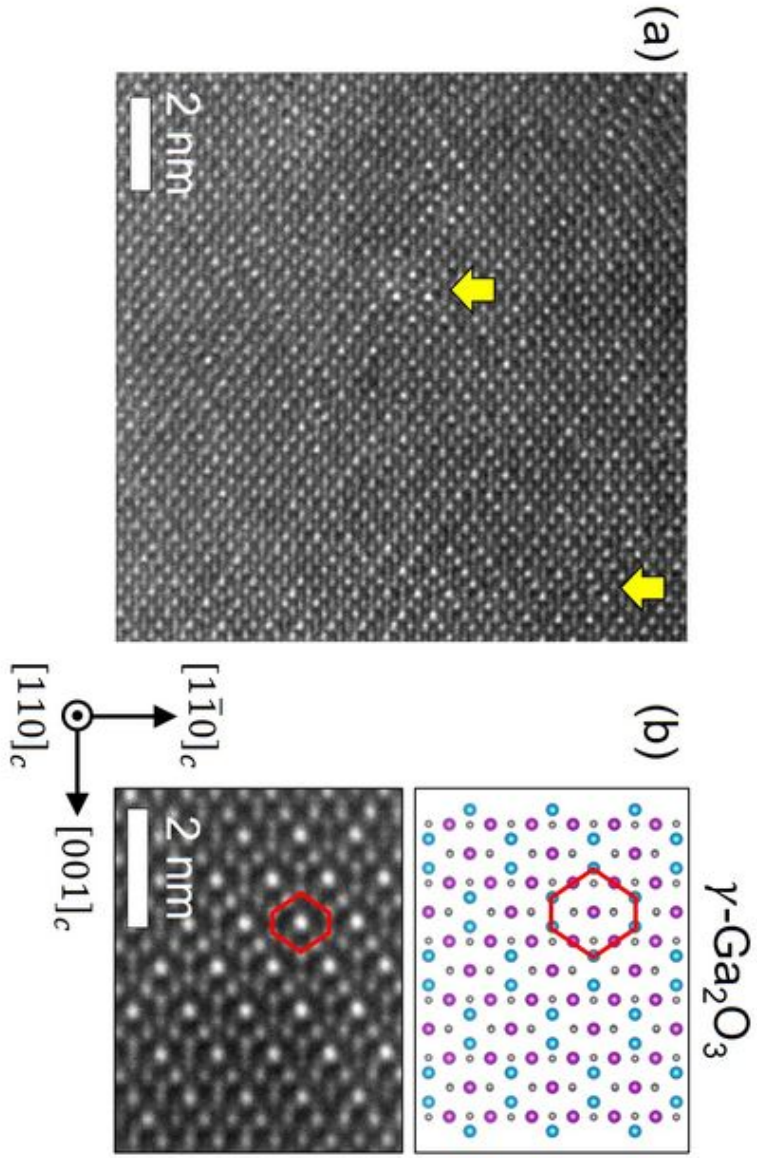

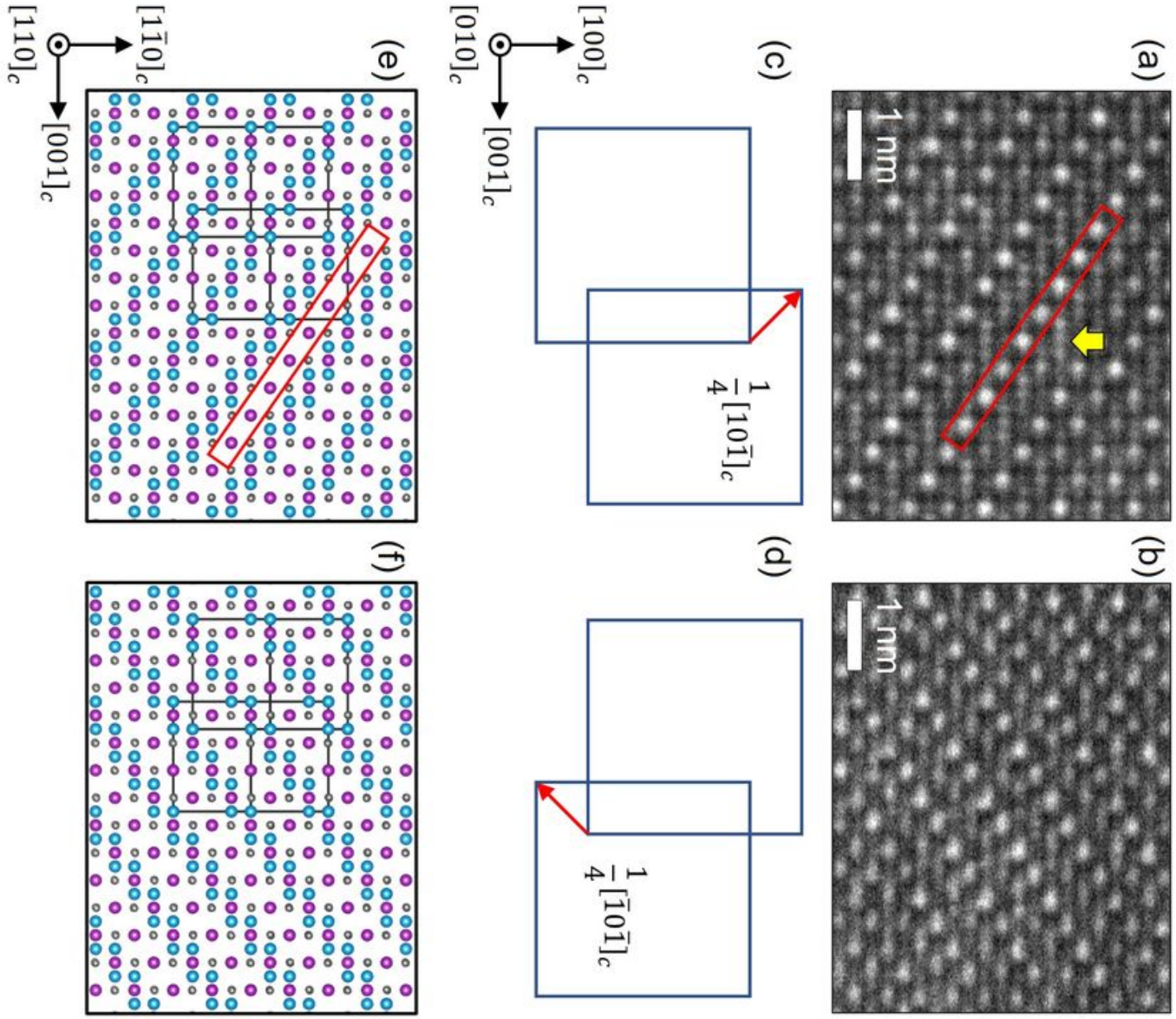

PLEASE CITE THIS ARTICLE AS DOI: 10.1063/5.0099915